



Adsorption and desorption behavior of titanium-decorated polycrystalline graphene toward hydrogen storage: a molecular dynamics study

Nitin Luhadiya¹ · S. I. Kundalwal¹ · S. K. Sahu¹

Received: 11 October 2021 / Accepted: 9 December 2021 / Published online: 18 December 2021
© The Author(s), under exclusive licence to Springer-Verlag GmbH, DE part of Springer Nature 2021

Abstract

The hydrogen adsorption and desorption capacity of polycrystalline graphene sheets (PGs) with and without titanium (Ti) decoration is investigated using molecular dynamics simulations. Interatomic interactions of PGs are modeled using Tersoff potential, and the remainder of interactions are calculated via Lennard–Jones potential. The effect of grain size and Ti concentration on the mechanical properties and hydrogen adsorption capacity of PGs is studied. The presence of grain boundaries in PGs reduces their mechanical properties, while the decoration of Ti adatoms does not significantly alter the mechanical properties of PGs. PGs showed a ~57% increase in the gravimetric density of H₂ at 300 K and 50 bar compared to the pristine graphene sheet. At 100 bar pressure, PGs with 1% Ti concentration achieved a gravimetric density of 9.9 wt.% and 3.2 wt.% at 77 and 300 K, respectively. In Ti-decorated PGs, the desorption curve follows the same path at 300 K as the adsorption curve with increasing Ti concentration, and the desorption curve diverges from the adsorption curve after 1.5% Ti concentration at 77 K. The potential use of the isosteric enthalpy of adsorption to determine the adsorbent's capability for adsorbing H₂ molecules is also discussed.

Keywords Polycrystalline graphene · Titanium decoration · Hydrogen adsorption and desorption · Potential energy distribution · Isosteric enthalpy of adsorption · Molecular dynamics

1 Introduction

Hydrogen, a potential alternative for future energy schemes, attracts a lot of attention due to its sustainability, high efficiency, and environmental friendliness compared to carbon-based fuels. Hydrogen in fuel cells has a wide range of applications, including portable power and backup power systems, additional power for trucks, ships, and aircraft, a primary power source for vehicles like forklifts, trucks, buses, and cars [1–5]. However, the safe, reliable, and efficient onboard storage of hydrogen in vehicles is still a challenge [6, 7]. An ideal hydrogen storage system should have high gravimetric density, fast kinetics, and reusability at room temperature [8]. Currently, hydrogen is

used as a liquid or gas in high-pressure tanks, which raises safety and economic concerns. An alternative method is solid-state storage, where the hydrogen molecules are bonded to the material by physical and chemical bonds. For solid-state storage, lightweight, porous materials with a high specific surface area are preferred to improve the hydrogen storage capacity. These materials adsorb hydrogen through different mechanisms, either by physical bonds (physisorption) or by chemical bonds (chemisorption). Adsorption through chemisorption is undesirable for hydrogen storage as it leads to chemical dissociation of the hydrogen molecule and firm binding of hydrogen, which cannot be released during the desorption process. Metal hydrides and complex hydrides store hydrogen with high gravimetric efficiency at ambient temperatures, but due to the strong binding of hydrogen, they have low reversibility, slow reaction kinetics, and a high dehydrogenation temperature [9, 10]. Binding energy higher than 0.6 eV/H₂ leads to chemical dissociation of the hydrogen molecule, which reduces the amount of usable hydrogen. For high gravimetric density and fast kinetics, the non-dissociative

✉ S. I. Kundalwal
kundalwal@iiti.ac.in

¹ Applied and Theoretical Mechanics (ATOM) Laboratory, Department of Mechanical Engineering, Indian Institute of Technology Indore, Simrol, Indore 453552, India

binding energy ranges between 0.1 and 0.6 eV/H₂ [11]. For this purpose, porous carbon nanostructures are emerging as potential candidates for hydrogen storage. One such material is graphene [12, 13], a single layer of carbon atoms arranged in a hexagonal lattice with a high elastic modulus (~ 1 TPa), high strength (~ 130 GPa) [14], large specific surface area (2630 m²/g) [15], and ease in tuning to enhance adsorption properties [16]. Pristine graphene sheets cannot bind sufficient hydrogen on their surface at ambient temperature due to low binding energy [17–19]. Carbon-based nanocomposites are also used in hydrogen storage systems as they are easy to modify with metals, metal oxides, and other organometallic frameworks [20–23]. Therefore, many theoretical and experimental studies have focused on increasing the hydrogen storage capacity of graphene. One of the most widely used methods is the functionalization of the surface of graphene, which leads to the tailoring of characteristics like the surface area, chemical reactivity, porosity, and interlayer spacing to enhance the adsorption capacity [24–27].

Experimental investigations have shown that large-area graphene films are polycrystalline, made up of small crystalline grains of different orientations joined by grain boundaries (GBs) [28]. The experimental study performed by Huang et al. [29] on polycrystalline graphene sheets (PGs) revealed that the presence of GBs reduces mechanical properties but does not alter electrical properties as drastically. Chen et al. [30] performed molecular dynamics simulations (MDS) to investigate the effect of the grain size, temperature, and strain rate on PGs. They showed that Young's modulus reduces by 65–82% and fracture strength reduces by 34–40% as the grain size in PGs decreases at room temperature. Alian et al. [31] investigated the mechanical properties and fracture behavior of polycrystalline carbon nanotubes (PCNT) with a variety of GBs morphology using MDS. They first created PCNT by rolling PG and reported that a crack initiates at GBs, and there is a strength reduction by 60% due to the presence of transverse GBs in the PCNT. GBs aligned with the axis of PCNT have the least effect on the mechanical properties compared to all other orientations of GBs. Izadifar et al. [32, 33] investigated the mechanical properties of PGs with nanopores doped with boron and nitrogen using MDS. They reported that (i) the ultimate failure strain of PGs increases with decreasing grain size, (ii) the doping of boron or nitrogen reduces the tensile strength of PGs, and (iii) nitrogen doping has a more severe effect compared to boron doping. Guo et al. [34] experimentally investigated the adsorption behavior of hydrogen at the interface of PGs and revealed that open edges and domain boundaries provide more active sites for adsorption and lower resistance for charge transfer. Also, the nanoscale features of nanostructured graphene provide excellent adhesion of hydrogen on the PGs.

Bhattacharya et al. [35] decorated graphene, h-BN, and BC₄N with titanium (Ti) atoms for high-capacity hydrogen storage using first-principles calculations. They reported a stable high adsorption capacity of hydrogen at room temperature, and that desorption occurs at a temperature of 700–800 K for graphene and h-BN sheets, but desorption for BC₄N occurs at 500–600 K. Park et al. [36] doped boron-substituted graphene sheets with lithium atoms to investigate the hydrogen adsorption capacity and reported a high adsorption capacity of 13.2 wt.% without any clustering of adatoms. An ab initio study performed by Wang et al. [37] on boron-substituted graphene uniformly decorated with sodium atoms showed a hydrogen storage capacity of 11.7 wt.% at 300 K. Lee et al. [38] doped nitrogen-decorated graphene with lithium for geometric stability and enhancement of hydrogen capacity using density functional theory (DFT) calculations. They observed cluster-free decoration of lithium atoms on nitrogen-doped graphene layers and found binding energy of hydrogen molecules in the range of 0.12–0.20 eV/H₂. The hydrogen adsorption capacity of Ti-doped graphyne under different external electric fields was investigated by Zhang et al. [39] using first principle calculations. They found that the interaction between Ti and H₂ molecules increases with the applied electric field. They also reported the adsorption of four hydrogen molecules on Ti-doped graphyne, and all are stored in molecular form. A DFT study performed by Lebon et al. [40] on graphene nanoribbons doped with Ti atoms showed non-dissociative adsorption of the hydrogen molecule. They reported that each doped Ti atom can adsorb up to four hydrogen molecules, showing an adsorption capacity beyond 6%. Yuan et al. [41] performed DFT simulations on porous graphene decorated with Ti atoms to calculate the hydrogen adsorption capacity. They reported that hydrogen molecules are adsorbed with a binding energy of –0.457 eV, and the gravimetric hydrogen storage capacity is 6.11 wt.%. Also, their study reported that six hydrogen molecules are adsorbed on both sides of the Ti-porous graphene system at 300 K. An experimental study performed by Goharibajestani et al. [42] for the hydrogen adsorption capacity of reduced graphene oxide decorated with different transition metal oxides revealed that the addition of TiO₂ results in the highest isosteric heat of adsorption of 13 kJ/mol for hydrogen. Rafique et al. [43] calculated the hydrogen adsorption capacity of Ti-doped double vacancy hexagonal boron nitride monolayered sheets using DFT. They found that only three H₂ molecules are attached on a single side of the sheet, whereas five molecules can be attached with high binding energy and thermodynamic stability on both sides of the sheet. Kag et al. [44] performed MDS for enhancement of the hydrogen adsorption capacity of graphene sheets via strain and defect engineering. They concluded that strained and defective sheets are more active for hydrogen adsorption and

sheets with 1% monovacancy defects at 100 bar pressure achieves 9.3 wt.% and 2.2 wt.% at 77 K and 300 K, respectively. Nuhnen and Janiak [45] analyzed the adsorption of isotherms of CO₂, SO₂, and H₂ gases at two temperatures on MOFs. They discussed multiple methods to calculate the isosteric enthalpy of adsorption at different but close temperature isotherms ≤ 20 K. Single-layer polycrystalline graphene nanosheet is not easy to synthesize, and multiple layers reduce the available surface area for adsorption. These sheets also oxidize quickly, hindering their hydrogen adsorption capacity and ability to bind metal decorations. Simulations of multilayer graphene sheets with the addition of oxygen to the system could also make it more realistic. Experimental investigations on polycrystalline graphene nanosheets have been widely investigated for various purposes, but authors couldn't find any study on their hydrogen adsorption capacity.

The literature on the fabrication of large-area graphene reveals that the GBs are wide-ranging in them, owing to inherent issues with fabrication techniques, surface energy, impurities, etc. [31, 34, 46, 47]. To the best of our knowledge, there has been no single attempt to study the adsorption and desorption behavior of PGs and Ti-decorated PGs toward hydrogen storage using MDS. The present work focused on studying the adsorption and desorption behavior, and showing a novel pathway to enhance the hydrogen adsorption capability of PGs by decorating Ti atoms via large-scale MDS. Fracture mechanics analysis of PGs and Ti-PGs is also carried out under uniaxial tensile loadings. The importance of the presence of inherent GBs and the domain sizes as well as the Ti atoms concentration, temperature, and pressure in determining the interactions between hydrogen gas and the graphene surface is considered. The isosteric enthalpy of adsorption for Ti-decorated PGs is also determined to analyze the mechanics of adsorption at different temperature ranges. The understanding of the interface properties between graphene, Ti, and H₂ molecule provides a wide range of possibilities for the use of Ti-graphene-based structures as a potential material for efficient hydrogen storage systems.

2 Methodology

Classical MDS is the most preferred technique for the simulation and characterization of nanomaterials. MDS allows for a comprehensive study of the interatomic interactions of various atomic species at an atomic scale using Newtonian mechanics with a time integration approach. Here, MDS are performed on systems of PGs with and without decoration of Ti atoms for investigating the hydrogen adsorption capacity of PG systems. All MDS were conducted via the

LAMMPS [48] software package based on classical molecular dynamics.

Our simulations consist of PGs created from a unit cell of graphene using Voronoi tessellation and Delaunay triangulation techniques [31]. Multiple PGs are created, with varying grain sizes calculated by $\sqrt{\frac{L^2}{N}}$ [33], where L is the length of the sheet and N is the number of grains. The misorientation angle of GBs varies during the synthesis of graphene; thus, misorientation angles were not controlled in this study, and randomly oriented PGs of various grain sizes were simulated. The PGs were then decorated with different concentrations of Ti atoms to study the doping effect on the strength under uniaxial tension and hydrogen adsorption capacities. Figure 1 shows the equilibrated structures of PG with a grain size of 4.47 nm and Ti-PGs with 1% Ti concentration.

To accurately perform MDS of hydrogen adsorption on PGs decorated with Ti atoms, the interatomic interactions of PGs atoms are described using the Tersoff potential [49], which was applied successfully in previous studies [50, 51]. The interactions between carbon atoms of PGs and Ti atoms are described using the Lennard–Jones (LJ) 12-6 potential. In this study, the diatomic hydrogen molecule is considered as a single entity. The interatomic interactions between hydrogen molecules (H₂) and Ti-PGs are also described using the LJ potential, as follows:

$$u_{ij} = 4\epsilon_{ij} \left[\left(\frac{\sigma_{ij}}{r} \right)^{12} - \left(\frac{\sigma_{ij}}{r} \right)^6 \right] \quad (1)$$

where u_{ij} is the pairwise interaction energy, and ϵ_{ij} and σ_{ij} are the well-depth energy and the distance at which the pair interaction energy goes to zero, respectively. The cut-off distance of 12 Å is chosen for LJ interactions. Table 1 describes the LJ potential parameters used in this study [52–55]. As previously reported [49], the force field utilized in this work was applied to carbon nanostructures. It was observed that no bonds are formed between the carbon structure and Ti-atoms, and hydrogen atoms are also physisorbed on Ti-graphene sheets. Thus, the current force field presents an accurate description for simulating the adsorption dynamics. The LJ parameters between different species are obtained using Lorentz–Berthelot mixing rules:

$$\epsilon_{ij} = \sqrt{\epsilon_{ii}\epsilon_{jj}}; \quad \sigma_{ij} = \frac{\sigma_{ii} + \sigma_{jj}}{2} \quad (2)$$

Tensile simulation tests on pristine graphene sheets in the armchair direction are performed. However, various factors like the strain rate, the direction of stress applied, and temperature influence the mechanical properties of graphene sheets; such effects are not considered for validation purposes. The tensile test simulation carried out herein provides the Young's modulus, fracture strength, and fracture

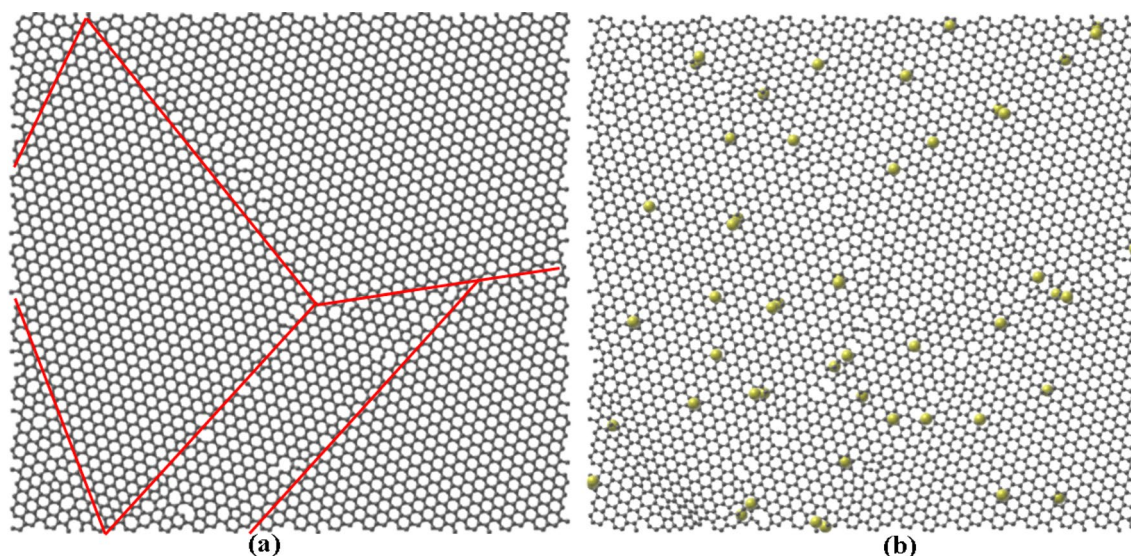


Fig. 1 **a** Polycrystalline graphene sheet [red lines indicate the GBs], and **b** polycrystalline graphene sheet decorated with randomly distributed titanium atoms. [Yellow Ti atoms; and gray C atoms]

Table 1 LJ interaction parameters for different atomic interactions

Parameter	H ₂ –H ₂	C–C	Ti–Ti
ϵ (kcal/mol)	0.067962	0.055641	0.5681
σ (nm)	0.296	0.340	0.268

strain of 857.9, 162.8, and 0.189 GPa, respectively, which is in good agreement with the previous study [56]. Thus, the above description of the interatomic potential is sufficient to proceed with the simulation of the Ti-PGs tensile test and hydrogen adsorption capacity investigation.

PGs with a grain size of 1–8 nm are modeled, and then these sheets are decorated with Ti atoms with a concentration up to 2.0%. These concentrations are a measure of the coverage of the Ti atoms on PGs. These sizes are chosen to optimize the computational time required with a large number of atoms in the system under consideration. Ti atoms are randomly placed above and below the PGs in the simulation box, with the Ti concentration up to 2.0%. The amount of Ti atoms to spread around the PGs depends on the adatoms concentration, given by

$$\rho(\%) = \frac{\text{Number of titanium atoms}}{\text{Number of carbon atoms in the PGs}} \times 100 \quad (3)$$

Figure 2 shows the simulation box with hydrogen molecules surrounding the Ti-decorated PGs. For simulating monolayer sheets, the PGs are placed in a box with a periodic boundary condition in all directions. The out-of-plane directions of Ti-PGs are kept large enough to avoid the interlayer interactions. A timestep of 0.5 fs was adopted, which is small enough to encapsulate accurate fracture

and adsorption dynamics. The conjugate gradient method was applied with an energy convergence of 10^{-10} to obtain energy-minimized systems. For a stress-free sheet, an equilibration run for 250 ps is performed under an isothermal and isobaric ensemble.

Tensile tests are performed at a temperature of 300 K and pressure of 1 bar, where the Nosé–Hoover thermostat and barostat control the temperature and pressure of the system, respectively. During the tensile test, a strain rate of 10^{-7} Å/fs was applied, and the stresses on the atomic structures were recorded every few timesteps. Atomic stresses on the sheet were estimated on the basis of the virial theorem. The average virial stress (σ) over volume Ω with a total number of atoms n^A is described by

$$\sigma = \frac{1}{\Omega} \left(\frac{1}{2} \sum_{\alpha=1}^{n^A} \sum_{\substack{\beta=1, \\ \beta \neq \alpha}}^{n^A} \mathbf{r}_{\alpha\beta} \otimes \mathbf{f}_{\alpha\beta} - \sum_{\alpha=1}^{n^A} m_{\alpha} \dot{\mathbf{u}}_{\alpha} \otimes \dot{\mathbf{u}}_{\alpha} \right) \quad (4)$$

where m_{α} is the mass of atom α ; \mathbf{r} is the position vector, \mathbf{f} is the force vector, and \mathbf{u}_{α} , $\dot{\mathbf{u}}_{\alpha}$ are the displacement and velocity vectors of atom α , respectively. The engineering strain is used for measuring deformation described by $\epsilon = \frac{\Delta L}{L_0}$, where ΔL defines the change in the length of the sheet upon deformation and L_0 is the original length of the sheet.

For hydrogen adsorption, grand canonical Monte Carlo (GCMC) simulations with an isothermal ensemble are performed, where hydrogen molecules are added into the system randomly at different locations in the simulation box. In GCMC simulations, the input parameters like the

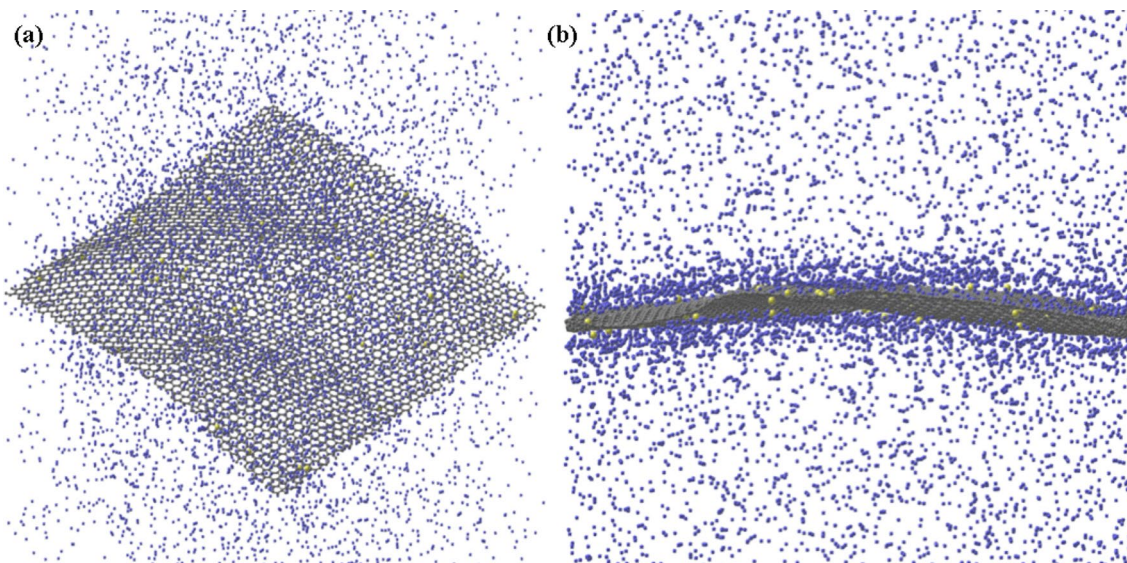


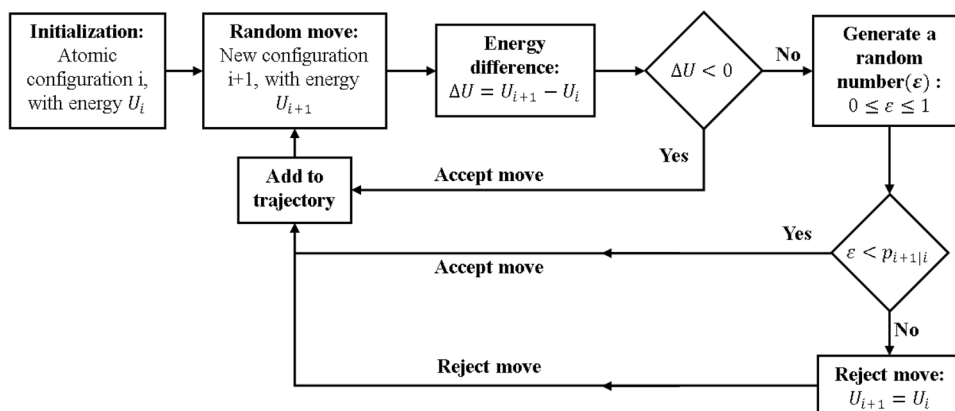
Fig. 2 System configuration of titanium-decorated polycrystalline graphene sheets: **a** isometric view and **b** side view. [Blue hydrogen atoms; yellow Ti atoms; and gray C atoms]

temperature and chemical potential (or pressure) of a fictitious gas reservoir are the known parameters, and the amount of gas in the system can be calculated. The amount of gas present in the simulation box is in equilibrium with the fictitious gas reservoir when its temperature and chemical potential (or pressure) become equal. The three operations in a GCMC simulation, such as insertion, deletion, and displacements, are performed with equal probabilities randomly. Figure 3 shows the steps involved in a typical Monte Carlo (MC) simulation where the acceptance and rejection of a random move is defined. The potential energy U of the system at the initial atomic configuration i is evaluated. Then, a random move is applied to the atoms, which corresponds to $i + 1$. If the energy of the system after this move is reduced, i.e. $U_{i+1} < U_i$, then the move is accepted. The probability of adding the new configuration to the trajectory after every MC move is given by $p_{i+1|i} = \exp\left(-\frac{\Delta U}{k_B T}\right)$, where

k_B is the Boltzmann constant. If $U_{i+1} > U_i$, then a random number ϵ is generated, where $0 < \epsilon < 1$. Now, if $\epsilon < p_{i+1|i}$, then the move is accepted; otherwise, the move is rejected. The amount of MC cycles is defined while running the simulations. The accepted moves are added to the trajectory, and the rejected moves are traced back to the previous state, and then they are also added to the trajectory, i.e., the same trajectory is added twice to obtain the correct probability. Finally, ensemble averages are calculated for every MC move.

After the GCMC run, a system equilibration is performed using the isothermal and isobaric ensemble at the desired temperature and pressure for 2 ns. A run time of 2 ns is sufficient to encapsulate adsorption dynamics at a specified temperature and pressure [57]. During adsorption simulations, the wt.% at each pressure is calculated with the adsorbed amount of hydrogen molecules on the

Fig. 3 Flow diagram of MC simulations



sheets, whereas, during desorption simulations, the sheet and hydrogen molecules system at 100 bar is brought down to the desired pressure to calculate the adsorption capacity. The hydrogen molecules that are adsorbed on the Ti-PGs are measured in wt.% calculated by

$$\text{wt.}\% = \frac{w_{\text{H}_2 - \text{adsorbed}}}{w_{\text{H}_2 - \text{adsorbed}} + w_C + w_{\text{Ti}}} \quad (5)$$

where $w_{\text{H}_2 - \text{adsorbed}}$ is the weight of the adsorbed hydrogen molecule, w_C and w_{Ti} are the weight of the carbon and Ti atoms present in the Ti-PGs, respectively. The number of adsorbed hydrogen molecules on the sheet is estimated using the potential energy distribution (PED) of atoms [57].

Hydrogen adsorption simulations are performed on Ti-PGs of different adatom concentrations at different temperatures and pressures ranging from 77 to 300 K and 0–100 bar, respectively. Adsorption isotherms at temperatures of 77, 97, 280, and 300 K are studied up to 100 bar pressure to calculate the isosteric enthalpy of adsorption (ΔH_{ads}). The Ti-PGs– H_2 interaction energy at a particular temperature is typically calculated from at least two adsorption isotherms obtained at very close temperatures (i.e., with a maximum difference of 20 K). The adsorption isotherms data from the MDS are fitted with the Toth isotherm [58]. Toth is an empirical model commonly used to describe the adsorbate adsorbent interactions for hydrogen adsorption with graphene [57]. The amount of adsorbed quantity using the Toth model is calculated by

$$\text{wt.} = \frac{\text{wt.}_m \cdot K \cdot p}{(1 + (Kp)^n)^{1/n}} \quad (6)$$

where wt._m is the constant reflecting the maximum adsorption capacity, K is the Toth constant representing the affinity of the adsorbent for the adsorbate, and n is the heterogeneity factor. The isosteric enthalpy of adsorption, ΔH_{ads} , is given by

$$\Delta H_{\text{ads}} = -RT^2 \left(\frac{\partial(\ln p)}{\partial T} \right)_{\text{wt.}_i} \quad (7)$$

The above equation is known as the Clausius–Clapeyron equation, where R is the universal gas constant, T is the temperature at which enthalpy is calculated, and p is the pressure at the same adsorbed quantity (wt.%) for different isotherms (i.e., isosteric pressures). To determine ΔH_{ads} , $\ln(p)$ against wt.% is plotted using the values from the modeled Toth isotherms at two close temperatures. The isosteric pressures are calculated from these plots and then, using Eq. (7), the enthalpy of adsorption is calculated.

3 Results and discussion

Comprehensive MD simulations are carried out to study the effect of GBs and Ti decoration on PGs' hydrogen storage capacity. Adsorption and desorption simulations are performed on PGs and Ti-PGs with varying grain sizes and adatom concentrations in this section. Also, the simulations are performed at high to low pressures and temperatures, enabling deep insight into the adsorption mechanics. The addition of Ti atoms on the PGs surface may produce a weak and unstable sheet. So firstly, PGs and Ti-PGs with varying concentrations and grain sizes are strained under tensile load until they fracture. Then, hybrid NVT-GCMC simulations are performed for investigating the hydrogen adsorption at different temperatures and pressures to obtain adsorption isotherms. The isosteric enthalpy of adsorption is determined at 77 and 300 K using the isosteric pressures from the adsorption isotherms.

Figure 4a shows the uniaxial tensile test of PGs with varying grain sizes at a temperature of 300 K. It can be observed that the fracture strength of PGs reduces as the grain size reduces, and a strength reduction of ~38% is observed from the pristine graphene at a grain size of 1 nm. The fracture strain of PGs increases with decreasing grain size; however, this value is still less than the pristine graphene, which is in good agreement with previous results [56]. Under the application of tensile loads, strained pristine sheets tend to adsorb slightly more hydrogen due to an increase in surface area and strong binding of stretched carbon atoms [40]. As evident from Fig. 4a, PGs fracture at lower strain than pristine thus strained PGs will not contribute significantly toward the hydrogen adsorption. The hydrogen adsorption capacity of PGs is also studied, as shown in Fig. 4b at 77 and 300 K, and pressures of 20 bar and 50 bar. The gravimetric density of the PGs at 77 K shows a small increase with decreasing grain size for both pressure conditions. Also, at 300 K, the wt.% shows a small increment with decreasing grain size. Adsorption simulation of PGs at the cryogenic temperature and pressures is performed to observe significant changes. The PGs with a 1 nm grain size at 300 K and 50 bar pressure show ~57% higher gravimetric density than the pristine sheet at the same temperature and pressure as found in an existing study [57]. Compared to the pristine sheet, the PGs show an increase in gravimetric density and a reduction in mechanical strength, but the strength of the PGs is still higher than most engineering materials. So, PGs with a grain size of 1 nm are used further in this study as the basis for further improving the hydrogen adsorption capacity.

Tensile tests are performed on functionalized PGs with a grain size of 1 nm and decorated with Ti atoms ranging

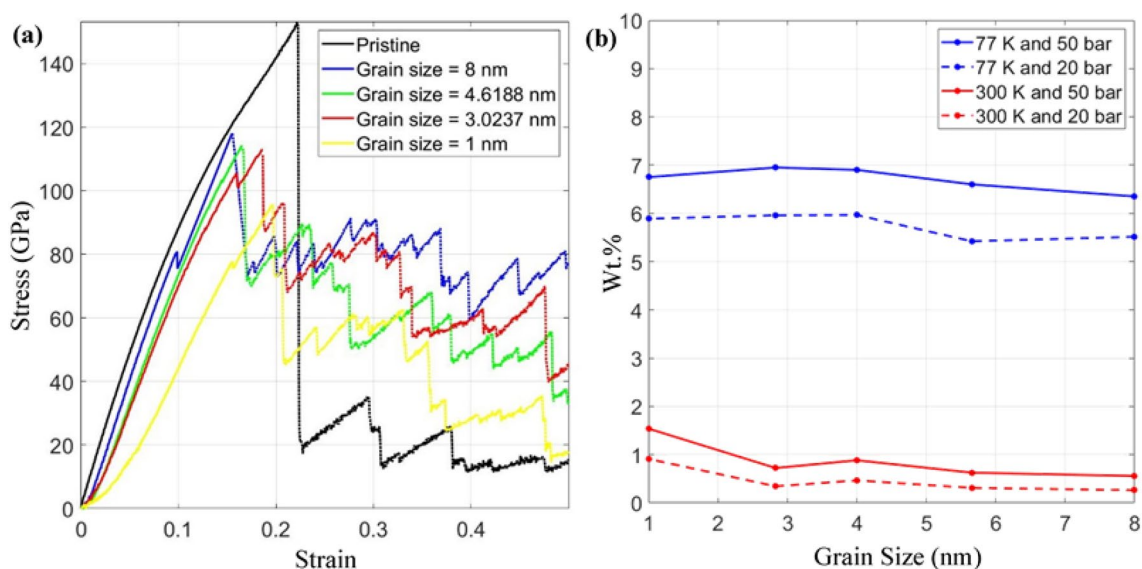


Fig. 4 **a** Uniaxial tensile test of PGs for different grain sizes and **b** hydrogen adsorption capacity of PGs with varying grain sizes at different temperatures and pressures

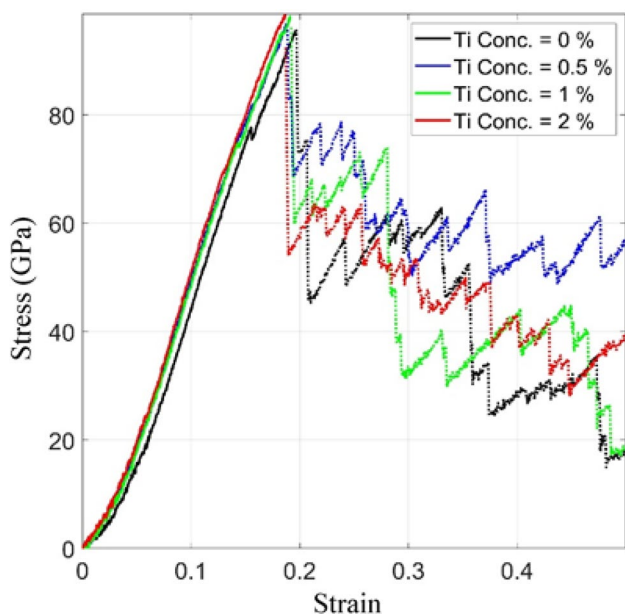


Fig. 5 The stress–strain curves of titanium-decorated PGs (1 nm grain size) for different titanium concentrations

from 0.5 to 2.0%. Figure 5 shows the stress–strain curves of the Ti-PGs with varying Ti concentrations. It can be observed from Fig. 5 that the concentration of Ti adatoms does not alter the PGs' mechanical properties. A small, insignificant increase in strength and decrease in strain is observed with Ti-decorated PGs as compared to non-decorated sheet. Thus, our findings indicate that Ti adatoms have no adverse effect on the mechanical properties of

PGs. Therefore, there are no restrictions on adding Ti atoms to enhance the adsorption capacity from a mechanical standpoint. The fracture mechanics of the PGs is also studied under tensile tests as shown in Fig. 6.

Figure 6a and b show the fracture of PGs with 1 nm grain size and Ti-PGs with 1 nm grain size (with 1% Ti concentration), respectively. It is observed that the GBs of the sheets are under more stress when the deformation is applied in the x -direction as compared to the inner part of the grain. Then, at a specific strain, a crack initiates almost perpendicular to the loading direction at the grain boundary and then propagates along the grain boundary; subsequently, the sheet ruptures along the armchair or zigzag path, keeping the crack almost perpendicular to the loading direction. It is noted that the Ti-decorated PGs also demonstrate similar fracture mechanics. Thus, this confirms our prediction that the Ti decoration has little to no effect on the mechanical properties of Ti-PGs. In PGs, GBs are a region containing multiple types of defects like 5-, 7-, 8-, and 9-membered rings, vacancies etc., thus possibly demonstrating reduced strength compared to the inner pristine part of the grain. Also, the GBs with an orientation perpendicular to the direction of the load bear more load than other GBs and are more prone to crack initiation.

The hydrogen adsorption capacity of PGs with 1 nm grain size decorated with varied concentrations of Ti atoms is determined using MDS. The hydrogen adsorption–desorption capacity of Ti-PGs is demonstrated in Fig. 7a and b at 77 and 300 K, respectively. The hydrogen adsorption capacity of Ti-PGs at 20, 50, and 100 bar is calculated for different Ti concentrations. The desorption capacity is obtained at 20

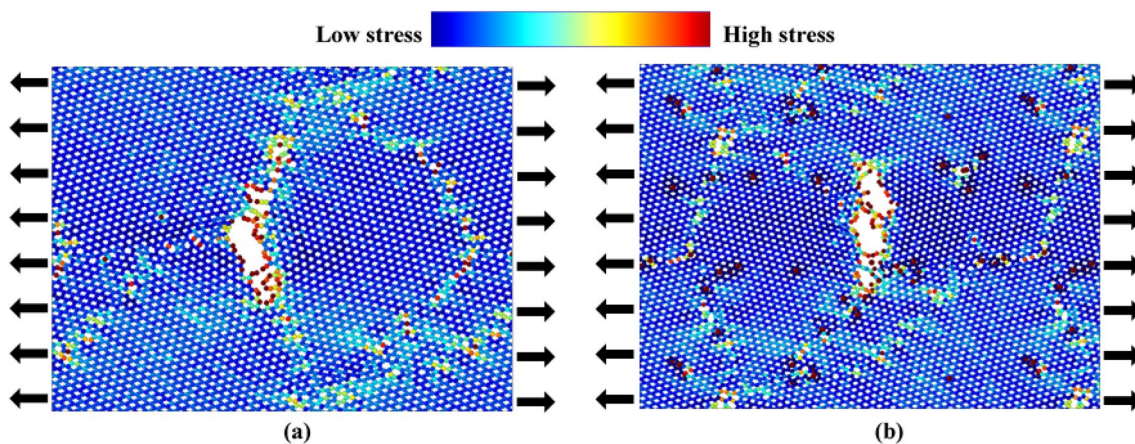


Fig. 6 Fracture of **a** polycrystalline graphene and **b** Ti-decorated polycrystalline graphene. Color coding shows the intensity of the stress. [Magenta Ti atoms]

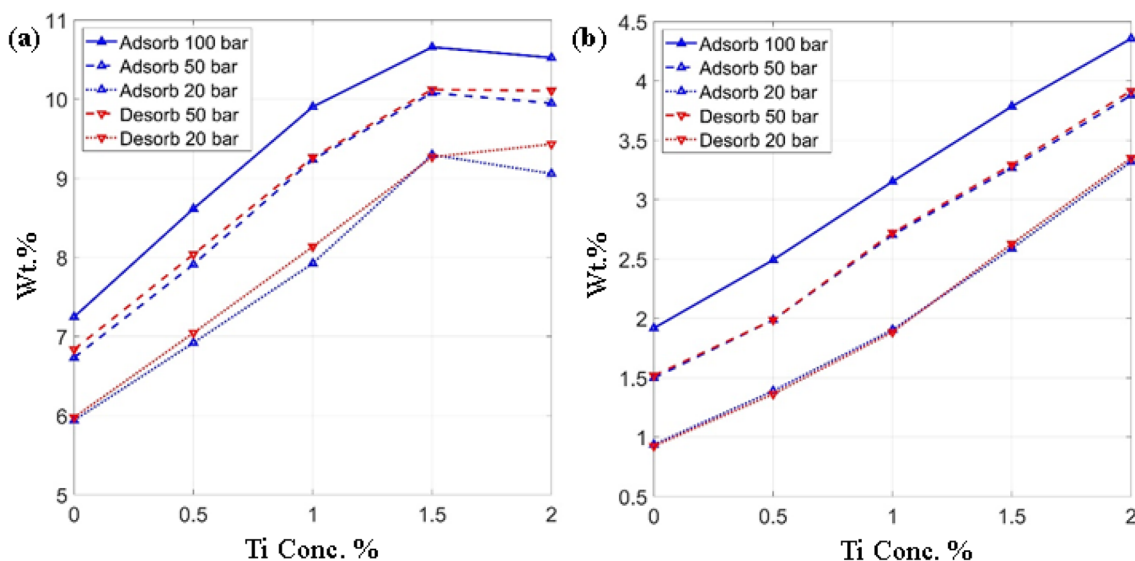


Fig. 7 Hydrogen adsorption and desorption capacity of Ti-PGs with 1 nm grain size at varying titanium concentrations at various pressures: **a** 77 K, and **b** 300 K temperatures

and 50 bar after equilibrating the system at 100 bar and then reducing to the desired pressure. It can be seen from Fig. 7a that the hydrogen adsorption capacity increases with the increase in Ti concentration up to 1.5%, and then decreases at 2% Ti concentration at 20, 50, and 100 bar pressures. A maximum adsorption capacity of 10.8 wt.% is achieved at 100 bar and 1.5% Ti concentration. Titanium adatom preferably attaches to the most active sites, and as the Ti concentration increases, the adatoms begin to agglomerate around these sites; thus, the reduction in hydrogen adsorption capacity at 2.0% Ti concentration and 77 K might be owed to (i) the decrease in the number of accessible Ti atoms for H_2 molecules as well as (ii) the increase in net mass with increasing Ti concentration. The desorption curves

follow a path similar to the adsorption curves, indicating a physisorbed state of H_2 molecules, but a lesser amount of hydrogen is released at 2% Ti concentration during the desorption with respect to the first adsorption, showing a stronger attraction of H_2 molecules to the Ti-PGs. At 300 K, there is a linear increase in the hydrogen adsorption capacity with increasing Ti concentration, as shown in Fig. 7b. A maximum H_2 adsorption capacity of 4.4 wt.% is achieved at 2% Ti concentration and 100 bar pressure. It is observed that there is a linear increase in adsorption capacities and the desorption curve at the temperature of 300 K, and pressures of 50 and 20 bar follow a path similar to the adsorption curves; thus, it indicates the physisorption of H_2 molecules. A high temperature of 300 K excites the Ti atoms and H_2

molecules with high velocities, hindering the agglomeration of Ti atoms and reducing the H₂ adsorption capacity of the Ti-PGs. The Ti-PGs show a higher adsorption capacity as compared to pristine sheets [57] at the same atmospheric conditions. The high adsorption capacity is due to the Kubas interaction [59, 60]. The σ bonding orbital of the H₂ molecule donates electron density to empty d-orbitals of Ti atoms with simultaneous π -back donations from the filled Ti d-orbital to the antibonding orbital of H₂ molecules. The respective loss and gain of electron density from bonding and antibonding orbitals result in elongation of the H₂ bonds, which reduces the interatomic repulsions and increases the adsorption capacity. Also, the carbon atoms neighboring the Ti adatoms tend to be more active for H₂ molecules adsorption. As discussed earlier, 1% Ti decoration does not lead to Ti atom agglomeration; therefore, Ti-PGs with 1% Ti concentrations will be used in further simulations.

Using MDS, the adsorption isotherms of H₂ molecules at temperatures of 77, 97, 280, and 300 K in the pressure range of 0–100 bar are demonstrated in Fig. 8a and b for Ti-PGs with 1 nm grain size and 1% Ti concentration. As discussed in the earlier section, the isosteric enthalpy of adsorption is calculated using two isotherms with a temperature difference ≤ 20 K. The data points from MDS are fitted with the Toth isotherm model using Eq. (6). A visual inspection and correlation coefficient (R^2) is used for the accuracy of the fit. All the fitted curves are in excellent agreement with the MDS data points, as shown in Fig. 8.

It can be observed from Fig. 8a that the H₂ adsorption capacities of Ti-PGs (with 1% Ti and 1 nm grain size) increase linearly at the start and then start to saturate between 40 and 50 bar pressure. The maximum adsorption

capacities at 77 and 97 K are 9.9 and 8.8 wt.%, respectively, at 100 bar pressure. Compared to the pristine graphene sheet at 77 K and 100 bar [57], a 46.67% increase in gravimetric density is observed. As discussed earlier, the desorption curves for Ti-PGs with 1 nm grain size and 1% Ti concentration follow a path similar to the adsorption curves; thus, the usable hydrogen, i.e., the hydrogen released (at 1 bar and 77 K) is $\sim 55\%$ more compared to the pristine sheet. The H₂ adsorption isotherms of Ti-PGs (with 1 nm grain size and 1% Ti concentration) at 280 and 300 K are depicted in Fig. 8b. The adsorption capacity at these temperatures also follows a very short linear path. The gravimetric densities of these sheets are 3.8 and 3.2 wt.% at 280 and 300 K, respectively, at 100 bar. The H₂ adsorption capacities of these sheets are ~ 4 times higher than the pristine graphene sheets [57]. The usable hydrogen is ~ 2.5 times higher than the pristine graphene sheets at 1 bar and 300 K. The H₂ adsorption capacity of Ti-PGs at 100 bar and 77 K is ~ 3 times higher as compared to 100 bar and 300 K. This is due to the higher kinetic energy of H₂ molecules at 300 K, which causes them to detach from the surface of Ti-PGs.

In order to study the energetics of H₂ adsorption on Ti-PGs, the isotherm obtained at low temperatures (77 and 97 K) and high temperatures (280 and 300 K) is used. The isosteric enthalpy of adsorption is determined using Eq. (7), where the natural log of pressures at specified wt.% is plotted with the respective wt.% as shown in Fig. 9a and b. Generally, the curve becomes linear over a wide range for gases with a low attraction to the adsorbent. The plot of the function $\ln p$ vs. wt.% is not a straight line, as depicted in Fig. 9, indicating a strong attraction of H₂ molecules on Ti-PGs. Thus, a Toth isotherm fitting for the MDS data points

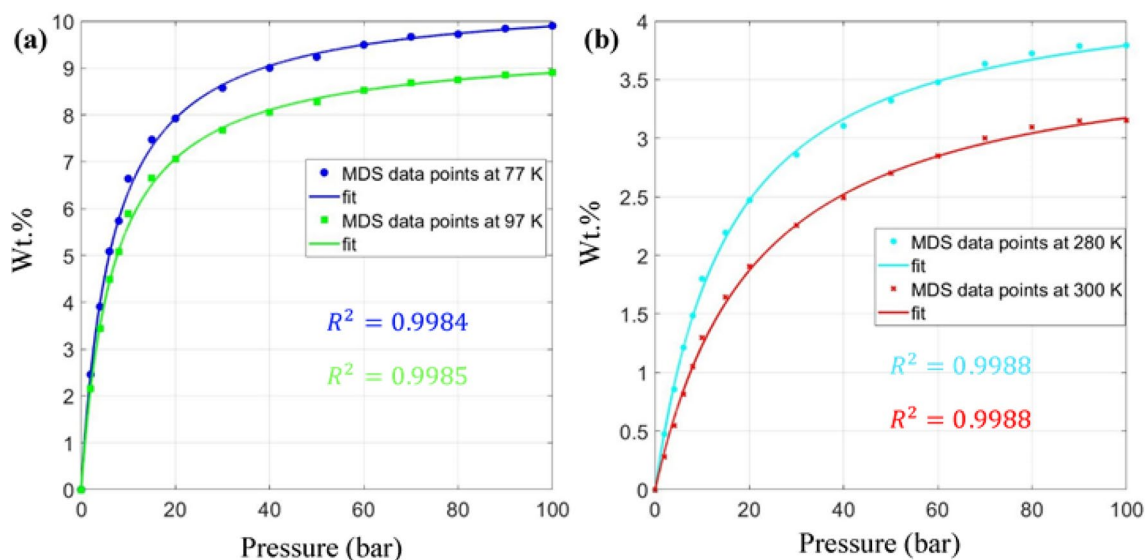


Fig. 8 Hydrogen adsorption isotherms of Ti-PGs with 1% Ti concentration at **a** low temperatures (77 and 97 K), and **b** high temperatures (280 and 300 K). MDS data points are fitted with Toth isotherm model

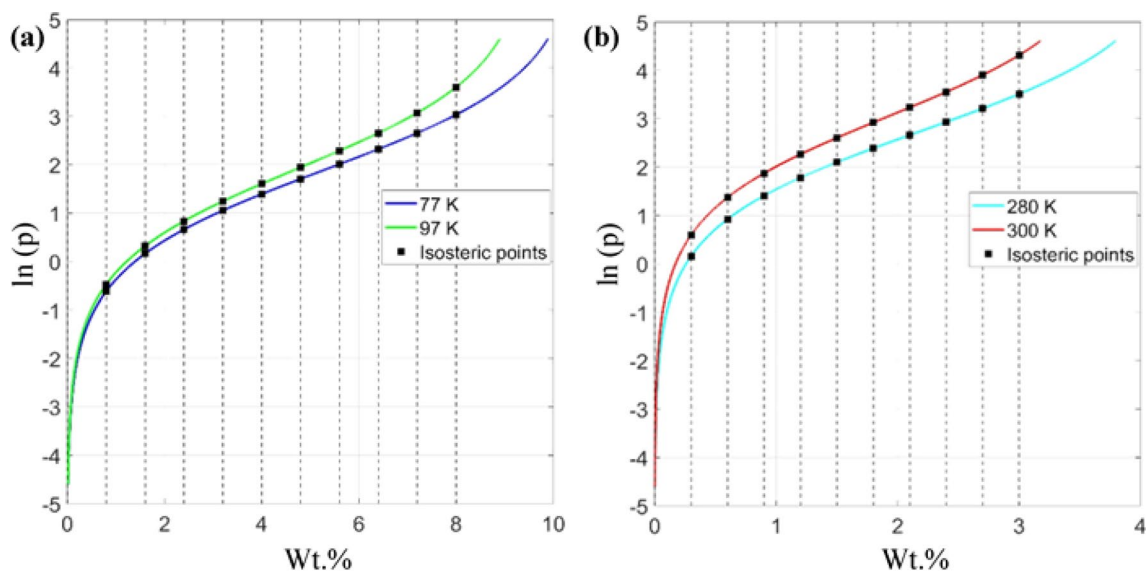


Fig. 9 Plot of logarithmic pressure against wt.% obtained from the isotherms of Ti-PGs at **a** low temperatures (77 K and 97 K) and **b** high temperatures (280 K and 300 K). Dashed lines are isosteric lines, and square markers are isosteric logarithmic pressures at different wt.%

is required to approximate the curve. The vertical lines are isosteric lines in Fig. 9, which indicate the logarithmic pressure values at constant wt.%. Multiple pairs of logarithmic pressure values at the two temperatures are noted at different wt.% in both Fig. 9(a) and 9(b). Ten data pairs are noted in both the figures to determine the adsorption enthalpy using Eq. 7.

The isosteric enthalpy of adsorption (ΔH_{ads}) determines the amount of heat released or absorbed during the adsorption process, and most of the adsorption processes

are exothermic. The variation of the enthalpy of adsorption (ΔH_{ads}) with wt.% is shown in Fig. 10a and b at 77 and 300 K, respectively. Conventionally, it is expected that the absolute value of ΔH_{ads} will reduce as the adsorption on the adsorbent increases because of the increasing intermolecular repulsions with increasing adsorbate density around the adsorbent surface, as evident from Fig. 10. The parameter ΔH_{ads} indirectly determines the strength of the adsorbent to attract the adsorbate. At low pressures, the adsorbate prefers to occupy the adsorption sites with the highest affinity,

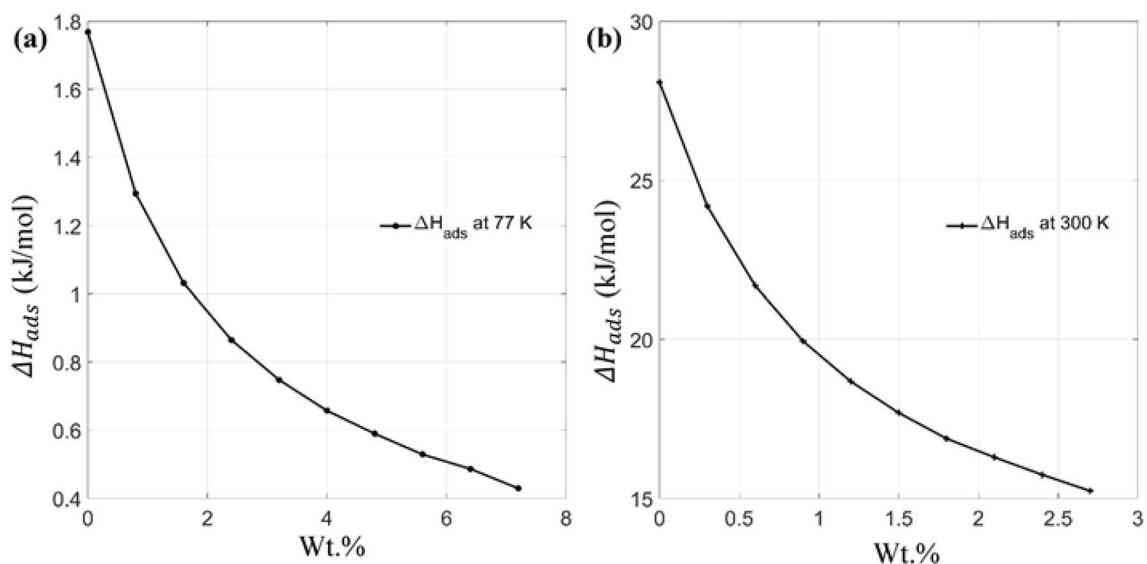


Fig. 10 Isosteric enthalpy of adsorption of H_2 for Ti-PGs **a** 77 K and, **b** 300 K

and these sites are associated with higher absolute ΔH_{ads} values at low loadings. The ΔH_{ads} at the start of adsorption, i.e., when the wt.% is zero, is called the enthalpy of adsorption at zero coverage (ΔH_{ads}^0). As shown in Fig. 10, the absolute value of ΔH_{ads}^0 is 1.78 and 28.5 kJ/mol at 77 and 300 K, respectively, indicating that the high adsorption sites are available at 300 K. Since the kinetic energy increases at high temperatures, the adsorbent's adsorption capacity reduces. However, the fewer molecules that are adsorbed at high temperatures have a very high ΔH_{ads} . The isosteric enthalpy of adsorption obtained for Ti-PGs is within the range of physisorption of hydrogen molecules. Physisorption allows fast kinetics and improved resistance to failure during multiple cycles of adsorption and desorption. This implies an efficient and reliable storage system is possible with the use of Ti-PGs.

4 Conclusions

In this study, the effect of GBs and Ti concentration on the hydrogen adsorption and desorption capacity of PGs is studied using MD simulations. A uniaxial tensile test of PG systems is also performed to analyze their fracture mechanics. The tensile tests on PGs with 1 nm grains show a maximum reduction in fracture strength by ~38% compared with the pristine graphene sheets, and Ti decoration on PGs shows no significant effect on the net strength. It is also observed that the crack initiation in PGs and Ti-PGs originates from the GBs that are vertical to the direction of the applied load. The H_2 adsorption capacity of PGs increases with the introduction of GBs; for example, the gravimetric density increases by ~57% compared to pristine graphene sheets at 300 K and 50 bar. The maximum adsorption capacity of PGs with 2% Ti decoration reaches 4.4 wt.% and shows no indication of Ti agglomeration at 300 K and 100 bar. It is observed that the desorption of PGs at 300 K follows the adsorption curve, indicating the physisorption of H_2 molecules. The maximum adsorption capacity at 280 and 300 K is 3.8 and 3.2 wt.%, respectively, at 100 bar. The adsorption capacity of Ti-PGs is ~4 times higher, and the usable hydrogen released is ~2.5 times higher than the pristine graphene sheet at 300 K. In the case of the lower temperature (77 K), Ti adatoms on PGs agglomerate and a significant reduction in gravimetric density at 2% Ti concentration is observed. The maximum H_2 adsorption capacity of Ti-PGs with 1.5% Ti concentration reaches 10.8 wt.% at 100 bar and 77 K. The adsorption isotherms of Ti-PGs with 1% Ti concentration at 77 and 97 K achieve a maximum adsorption capacity of about 9.9 and 8.8 wt. %, respectively, at 100 bar, and start to saturate at 40–50 bar pressure. Compared to the pristine graphene sheet at 77 K, the adsorption capacity of Ti-PGs with 1 nm grain size and 1% Ti concentration increases by ~46.67%, and the

usable hydrogen released at 1 bar is raised by ~55%. The absolute value of ΔH_{ads} decreases with increasing adsorption of H_2 , indicating a stronger preference of H_2 for adsorption sites with higher enthalpy. Unlike pristine graphene, a certain amount of Ti adatoms adhere to polycrystalline graphene sheets without clustering and can significantly improve their hydrogen adsorption capacity. There is also a strong indication of the physisorption of hydrogen molecules which helps in the fast kinetics of adsorption and desorption. Thus, the decoration of Ti atoms on polycrystalline graphene sheets shows a significant improvement in hydrogen carrying capacity. For developing an onboard hydrogen storage system, Ti-PGs at room temperature is a good candidate, but large amounts of graphene samples would be required. Currently, this is not economical, but with technological advances, the costs may go down, and future research in this direction will surely pave the way for a feasible storage system.

Acknowledgements This work is supported by the Department of Science and Technology (DST), Ministry of Science and Technology, Government of India. Authors SIK and SKS have received a research grant from the DST (DST/TMD/HFC/2K18/88). Author NL acknowledges the support from the Prime Minister's Research Fellows (PMRF) Program, Ministry of Education, Government of India (PMRF-192002-780).

Declarations

Conflict of interest The authors declared that they have no conflicts of interest in this work.

References

1. L. Schlapbach, A. Züttel, Hydrogen-storage materials for mobile applications. *Nature* **414**(6861), 353–358 (2001). <https://doi.org/10.1038/35104634>
2. G.W. Crabtree, M.S. Dresselhaus, M.V. Buchanan, The hydrogen economy. *Phys. Today* **57**(12), 39–44 (2004). <https://doi.org/10.1063/1.1878333>
3. A. Léon, Introduction. *Hydrogen Technol.* **1**, 11–13 (2008). https://doi.org/10.1007/978-3-540-69925-5_1
4. L. Schlapbach, Hydrogen-fuelled vehicles. *Nature* **460**(7257), 809–811 (2009). <https://doi.org/10.1038/460809a>
5. K. Mazloomi, C. Gomes, Hydrogen as an energy carrier: prospects and challenges. *Renew. Sustain. Energy Rev.* **16**(5), 3024–3033 (2012). <https://doi.org/10.1016/j.rser.2012.02.028>
6. P. Jena, Materials for hydrogen storage: Past, present, and future. *J. Phys. Chem. Lett.* **2**(3), 206–211 (2011). <https://doi.org/10.1021/jz1015372>
7. A. Léon, Hydrogen Storage. *Hydrogen Technol.* **3**, 81–128 (2008). https://doi.org/10.1007/978-3-540-69925-5_3
8. J. Li, T. Furuta, H. Goto, T. Ohashi, Y. Fujiwara, S. Yip, Theoretical evaluation of hydrogen storage capacity in pure carbon nanostructures. *J. Chem. Phys.* **119**(4), 2376–2385 (2003). <https://doi.org/10.1063/1.1582831>
9. N.A.A. Rusman, M. Dahari, A review on the current progress of metal hydrides material for solid-state hydrogen storage

- applications. *Int. J. Hydrogen Energy* **41**(28), 12108–12126 (2016). <https://doi.org/10.1016/j.ijhydene.2016.05.244>
10. E. Boateng, A. Chen, Recent advances in nanomaterial-based solid-state hydrogen storage. *Mater. Today Adv.* **6**, 100022 (2020). <https://doi.org/10.1016/j.mtadv.2019.100022>
 11. K.S. Chan, M.A. Miller, X. Peng, First-principles computational study of hydrogen storage in silicon clathrates. *Mater. Res. Lett.* **6**(1), 72–78 (2018). <https://doi.org/10.1080/21663831.2017.1396261>
 12. K.S. Novoselov, A.K. Geim, S.V. Morozov, D. Jiang, Y. Zhang, S.V. Dubonos, I.V. Grigorieva, A.A. Firsov, Electric field in atomically thin carbon films. *Science* **306**(5696), 666–669 (2004). <https://doi.org/10.1126/science.1102896>
 13. M. Pumera, Graphene-based nanomaterials for energy storage. *Energy Environ. Sci.* **4**(3), 668–674 (2011). <https://doi.org/10.1039/c0ee00295j>
 14. C. Lee, X. Wei, J.W. Kysar, J. Hone, Measurement of the elastic properties and intrinsic strength of monolayer graphene. *Science* **321**(5887), 385–388 (2008). <https://doi.org/10.1126/science.1157996>
 15. Y. Zhu, S. Murali, W. Cai, X. Li, J.W. Suk, J.R. Potts, R.S. Ruoff, Graphene and graphene oxide: Synthesis, properties, and applications. *Adv. Mater.* **22**(35), 3906–3924 (2010). <https://doi.org/10.1002/adma.201001068>
 16. S. Patchkovskii, J.S. Tse, S.N. Yurchenko, L. Zhechkov, T. Heine, G. Seifert, Graphene nanostructures as tunable storage media for molecular hydrogen. *Proc. Natl. Acad. Sci. U.S.A.* **102**(30), 10439–10444 (2005). <https://doi.org/10.1073/pnas.0501030102>
 17. Y. Okamoto, Y. Miyamoto, Ab initio investigation of physisorption of molecular hydrogen on planar and curved graphenes. *J. Phys. Chem. B* **105**(17), 3470–3474 (2001). <https://doi.org/10.1021/jp003435h>
 18. T. Heine, L. Zhechkov, G. Seifert, Hydrogen storage by physisorption on nanostructured graphite platelets. *Phys. Chem. Chem. Phys.* **6**(5), 980–984 (2004). <https://doi.org/10.1039/b316209e>
 19. V. Tozzini, V. Pellegrini, Reversible hydrogen storage by controlled buckling of graphene layers. *J. Phys. Chem. C* **115**(51), 25523–25528 (2011). <https://doi.org/10.1021/jp208262r>
 20. S.I. Kundalwal, M.C. Ray, Shear lag analysis of a novel short fuzzy fiber-reinforced composite. *Acta Mech.* **225**(9), 2621–2643 (2014). <https://doi.org/10.1007/S00707-014-1095-3>
 21. S.I. Kundalwal, M.C. Ray, S.A. Meguid, Shear lag model for regularly staggered short fuzzy fiber reinforced composite. *ASME J. Appl. Mech.* **81**(9), 091001 (2014). <https://doi.org/10.1115/1.4027801>
 22. S.I. Kundalwal, M.C. Ray, Improved thermoelastic coefficients of a novel short fuzzy fiber-reinforced composite with wavy carbon nanotubes. *J. Mech. Mater. Struct.* **9**(1), 1–25 (2014). <https://doi.org/10.2140/JOMMS.2014.9.1>
 23. S.I. Kundalwal, M.C. Ray, Thermoelastic properties of a novel fuzzy fiber-reinforced composite. *ASME J. Appl. Mech.* **80**(6), 061011 (2013). <https://doi.org/10.1115/1.4023691/370366>
 24. B. Szczeniński, J. Choma, M. Jaroniec, Gas adsorption properties of graphene-based materials. *Adv. Coll. Interface. Sci.* **243**, 46–59 (2017). <https://doi.org/10.1016/j.cis.2017.03.007>
 25. H.G. Shiraz, O. Tavakoli, Investigation of graphene-based systems for hydrogen storage. *Renew. Sustain. Energy Rev.* **74**, 104–109 (2017). <https://doi.org/10.1016/j.rser.2017.02.052>
 26. K.K. Gangu, S. Maddila, S.B. Mukkamala, S.B. Jonnalagadda, Characteristics of MOF, MWCNT and graphene containing materials for hydrogen storage: A review. *J. Energy Chem.* **30**, 132–144 (2019). <https://doi.org/10.1016/j.jechem.2018.04.012>
 27. V. Jain, B. Kandasubramanian, Functionalized graphene materials for hydrogen storage. *J. Mater. Sci.* **55**(5), 1865–1903 (2020). <https://doi.org/10.1007/s10853-019-04150-y>
 28. O.V. Yazyev, Y.P. Chen, Polycrystalline graphene and other two-dimensional materials. *Nat. Nanotechnol.* **9**(10), 755–767 (2014). <https://doi.org/10.1038/nnano.2014.166>
 29. P.Y. Huang, C.S. Ruiz-Vargas, Z.A.M. Van Der, W.S. Whitney, M.P. Levendorf, J.W. Kevek, S. Garg, J.S. Alden, C.J. Hustedt, Y. Zhu et al., Grains and grain boundaries in single-layer graphene atomic patchwork quilts. *Nature* **469**(7330), 389–392 (2011). <https://doi.org/10.1038/nature09718>
 30. M.Q. Chen, S.S. Quek, Z.D. Sha, C.H. Chiu, Q.X. Pei, Y.W. Zhang, Effects of grain size, temperature and strain rate on the mechanical properties of polycrystalline graphene - A molecular dynamics study. *Carbon* **85**, 135–146 (2015). <https://doi.org/10.1016/j.carbon.2014.12.092>
 31. A.R. Alian, S.A. Meguid, S.I. Kundalwal, Unraveling the influence of grain boundaries on the mechanical properties of polycrystalline carbon nanotubes. *Carbon* **125**, 180–188 (2017). <https://doi.org/10.1016/j.carbon.2017.09.056>
 32. M. Izadifar, R. Abadi, A. Namazian, T. Rabczuk, Investigation into the effect of doping of boron and nitrogen atoms in the mechanical properties of single-layer polycrystalline graphene. *Comput. Mater. Sci.* **138**, 435–447 (2017). <https://doi.org/10.1016/j.commatsci.2017.06.038>
 33. M. Izadifar, R. Abadi, A.H. Nezhad Shirazi, N. Alajlan, T. Rabczuk, Nanopores creation in boron and nitrogen doped polycrystalline graphene: A molecular dynamics study. *Physica E* **99**, 24–36 (2018). <https://doi.org/10.1016/j.physe.2017.12.036>
 34. Y. Guo, D.H. Seo, J. Hong, D. Su, H. Wang, J. Zheng, X. Li, A.B. Murphy, K. Ostrikov K (Ken), Controlling the adsorption behavior of hydrogen at the interface of polycrystalline CVD graphene. *Int. J. Hydrogen Energy* **43**(41):18735–18744 (2018). <https://doi.org/10.1016/j.ijhydene.2018.07.204>
 35. S. Bhattacharya, C. Majumder, G.P. Das, Ti-decorated BC4N sheet: a planar nanostructure for high-capacity hydrogen storage. *J. Phys. Chem. C* **113**(36), 15783–15787 (2009). <https://doi.org/10.1021/jp905853x>
 36. H.L. Park, S.C. Yi, Y.C. Chung, Hydrogen adsorption on Li metal in boron-substituted graphene: An ab initio approach. *Int. J. Hydrogen Energy* **35**(8), 3583–3587 (2010). <https://doi.org/10.1016/j.ijhydene.2010.01.073>
 37. F.D. Wang, F. Wang, N.N. Zhang, Y.H. Li, S.W. Tang, H. Sun, Y.F. Chang, R.S. Wang, High-capacity hydrogen storage of Na-decorated graphene with boron substitution: First-principles calculations. *Chem. Phys. Lett.* **555**, 212–216 (2013). <https://doi.org/10.1016/j.cplett.2012.11.015>
 38. S. Lee, M. Lee, H. Choi, D.S. Yoo, Y.C. Chung, Effect of nitrogen induced defects in Li dispersed graphene on hydrogen storage. *Int. J. Hydrogen Energy* **38**(11), 4611–4617 (2013). <https://doi.org/10.1016/j.ijhydene.2013.01.180>
 39. L. Zhang, S. Zhang, P. Wang, C. Liu, S. Huang, H. Tian, The effect of electric field on Ti-decorated graphyne for hydrogen storage. *Comput. Theor. Chem.* **1035**, 68–75 (2014). <https://doi.org/10.1016/j.comptc.2014.02.032>
 40. A. Lebon, J. Carrete, L. J. Gallego, A. Vega A. Ti-decorated zigzag graphene nanoribbons for hydrogen storage. A van der Waals-corrected density-functional study. *Int. J. Hydrogen Energy* **40**(14):4960–4968 (2018). <https://doi.org/10.1016/j.ijhydene.2014.12.134>
 41. L. Yuan, L. Kang, Y. Chen, D. Wang, J. Gong, C. Wang, M. Zhang, X. Wu, Hydrogen storage capacity on Ti-decorated porous graphene: First-principles investigation. *Appl. Surf. Sci.* **434**, 843–849 (2018). <https://doi.org/10.1016/j.apsusc.2017.10.231>
 42. Z. Goharibajestani, A. Yürüm, Y. Yürüm, Effect of transition metal oxide nanoparticles on gas adsorption properties of graphene nanocomposites. *Appl. Surf. Sci.* **475**, 1070–1076 (2019). <https://doi.org/10.1016/j.apsusc.2019.01.052>

43. M. Rafique, M.A. Uqaili, N.H. Mirjat, M.A. Tunio, Y. Shuai, Ab-initio investigations on titanium (Ti) atom-doped divacancy monolayer h-BN system for hydrogen storage systems. *Physica E* **109**, 169–178 (2019). <https://doi.org/10.1016/j.physe.2019.01.015>
44. D. Kag, N. Luhadiya, N.D. Patil, S.I. Kundalwal, Strain and defect engineering of graphene for hydrogen storage via atomistic modelling. *Int. J. Hydrogen Energy* **46**(43), 22599–22610 (2021). <https://doi.org/10.1016/j.ijhydene.2021.04.098>
45. A. Nuhnen, C. Janiak, A practical guide to calculate the isosteric heat/enthalpy of adsorption via adsorption isotherms in metal-organic frameworks. MOFs. *Dalton Trans.* **49**(30), 10295–10307 (2020). <https://doi.org/10.1039/D0DT01784A>
46. Y. Wei, C. Jiang, Y. Zhang, X. Li, L. Zhang, P. Wang, Y. Fang, Investigation of photocatalysis reactions on the single-crystal and polycrystalline graphenes. *Spectrochim. Acta Part A Mol. Biomol. Spectrosc.* **251**, 119441 (2021). <https://doi.org/10.1016/J.SAA.2021.119441>
47. J.S. Roh, J.K. Jang, N. Kwon, S. Bok, Y.J. Kim, C. Jeon, H.W. Yoon, H.W. Kim, B. Lim, H.B. Park, Macroscopic properties of single-crystalline and polycrystalline graphene on soft substrate for transparent electrode applications. *Carbon* **178**, 181–189 (2021). <https://doi.org/10.1016/J.CARBON.2021.02.097>
48. S. Plimpton, Fast parallel algorithms for short-range molecular dynamics. *J. Comput. Phys.* **117**(1), 1–19 (1995). <https://doi.org/10.1006/jcph.1995.1039>
49. J. Tersoff, Modeling solid-state chemistry: Interatomic potentials for multicomponent systems. *Phys. Rev. B* **39**(8), 5566–5568 (1989). <https://doi.org/10.1103/PhysRevB.39.5566>
50. S.I. Kundalwal, V.K. Choyal, N. Luhadiya, V. Choyal, Effect of carbon doping on electromechanical response of boron nitride nanosheets. *Nanotechnology* **31**(40), 405710 (2020). <https://doi.org/10.1088/1361-6528/ab9d43>
51. S.I. Kundalwal, V.K. Choyal, V. Choyal, S.K. Nevhal, N. Luhadiya, Enhancement of piezoelectric and flexoelectric response of boron nitride sheet superlattices via interface and defect engineering. *Physica E* **127**, 114563 (2021). <https://doi.org/10.1016/j.physe.2020.114563>
52. B. Faria, C. Guarda, N. Silvestre, J.N.C. Lopes, CNT-reinforced iron and titanium nanocomposites: Strength and deformation mechanisms. *Compos. B Eng.* **187**, 107836 (2020). <https://doi.org/10.1016/j.compositesb.2020.107836>
53. S. Zhen, G.J. Davies, Calculation of the Lennard-Jones–m potential energy parameters for metals. *Phys. Status Solidi (a)* **78**(2), 595–605 (1983). <https://doi.org/10.1002/pssa.2210780226>
54. R.F. Cracknell, Molecular simulation of hydrogen adsorption in graphitic nanofibres. *Phys. Chem. Chem. Phys.* **3**(11), 2091–2097 (2001). <https://doi.org/10.1039/b100144m>
55. S. Chu, L. Hu, X. Hu, M. Yang, J. Deng, Titanium-embedded graphene as high-capacity hydrogen-storage media. *Int. J. Hydrogen Energy* **36**(19), 12324–12328 (2011). <https://doi.org/10.1016/j.ijhydene.2011.07.015>
56. Z. Yang, Y. Huang, F. Ma, Y. Sun, K. Xu, P.K. Chu, Temperature and strain-rate effects on the deformation behaviors of nano-crystalline graphene sheets. *Euro. Phys. J. B* **88**, 135 (2015). <https://doi.org/10.1140/epjb/e2015-50850-x>
57. N. Luhadiya, S.I. Kundalwal, S.K. Sahu, Investigation of hydrogen adsorption behavior of graphene under varied conditions using a novel energy-centered method. *Carbon Lett.* **31**, 655–666 (2021). <https://doi.org/10.1007/s42823-021-00236-3>
58. J. Tóth, Calculation of the BET-compatible surface area from any Type I isotherms measured above the critical temperature. *J. Colloid Interface Sci.* **225**(2), 378–383 (2000). <https://doi.org/10.1006/jcis.2000.6723>
59. T.K.A. Hoang, D.M. Antonelli, Exploiting the Kubas Interaction in the Design of Hydrogen Storage Materials. *Adv. Mater.* **21**(18), 1787–1800 (2009). <https://doi.org/10.1002/ADMA.200802832>
60. J. Skipper C V., Ahmad Hamaed, M. Antonelli D, Nikolas Kaltsoyannis. The Kubas interaction in M(ii) (M = Ti, V, Cr) hydrazine-based hydrogen storage materials: a DFT study. *Dalton Trans.* **41**(28):8515–8523 (2012). <https://doi.org/10.1039/C2DT30383C>

Publisher's Note Springer Nature remains neutral with regard to jurisdictional claims in published maps and institutional affiliations.